Probing signal design for enhanced damping estimation in power networks

Sjoerd Boersma, Xavier Bombois, Luigi Vanfretti, Juan-Carlos Gonzalez-Torres, Abdelkrim Benchaib

Probing Signal Design for Enhanced Damping Estimation in Power Networks

Sjoerd Boersma[1], Xavier Bombois[2,3], Luigi Vanfretti[4], Juan-Carlos Gonzalez-Torres[1], Abdelkrim Benchaib[1]

Abstract

Electromechanical oscillations are inherent to power networks. Although it is possible to partially damp these oscillations, it is impossible to eliminate them completely. This oscillatory behavior can lead to major breakdowns in power networks, especially when the damping is relatively low. It is therefore important to provide accurate estimations of the network's damping values. These estimation can be obtained via system identification for which a probing signal needs to be designed. This paper presents a framework for designing a specific probing signal that is able to provide accurate damping estimations with a user-defined variance. A power spectrum of the probing signal is determined by solving an optimization problem with Linear Matrix Inequality constraints. The objective function is defined as a weighted sum of the probing signal's power and a level of disturbance caused by probing the network. A desired level of the damping estimation's variance is set as a constraint. The time-domain realization of the obtained power spectrum is described by a multisine, which is the actual probing signal applied to the network. The employed framework is demonstrated through nonlinear simulations using the Kundur with an embedded HVDC link and NORDIC 44 networks.

Keywords: damping estimation, system identification, experiment design, power networks

[1]Supergrid-Institute (corresponding author: sjoerd.boersma@supergrid-institute.com)
[2]Laboratoire Ampère, Ecole Centrale de Lyon, Université de Lyon, 36 avenue Guy de Collongue, Ecully, France
[3]Centre National de la Recherche Scientifique (CNRS), France
[4]Rensselaer Polytechnic Institute

1. Introduction

Accurate monitoring of electromechanical oscillations in near real-time is one of the most important functions of a wide area monitoring system [1]. Oscillations are monitored by continuously estimating the frequencies and damping ratios of dominant electromechanical modes. These are referred to as critical system modes and, in normal operation, are damped enough such that no overly large oscillations occur. However, the damping ratios of critical modes change over time due to, among others, disturbances in the network. It is possible that such a disturbance renders these damping ratios too low. Consequently, large oscillations and a potential blackout of the network occurs [2, 3]. It is thus important to continuously provide an accurate damping estimation so that, when this crosses a specific lower bound, corrective actions can be applied [4]. This prevents major oscillations and even system instabilities [5].

The described approaches in the literature that provide a continuous near real-time damping estimation can roughly be divided into two categories. The first category only uses the power system's ambient response. This occurs when the network is in equilibrium and is due to random load changes. This type of excitation is always present in a network and should therefore be accounted for in the damping estimation method. In general, ambient excitation is relatively low, which (for acceptable experiment lengths) results in estimations with relatively high variances. In the second category, the network is excited with a probing signal (for example by using a controllable power electronics device) and the successive response is measured. Then, both the probing signal and successive response are used for estimation.

The approach employed in this work is placed in the second category and have their theoretical underpinnings in the field of system identification. Results that belong to this category are found in [6, 7, 8, 9] and an overview is found in [10]. In [6], injected noise is produced by random load switching and a frequency domain identification technique is used to estimate the network's

behavior. In [7], several manually chosen probing signals are injected in the network and corresponding damping estimations are compared. In [8], different manually chosen sinusoidal probing signals are applied to a real-world network in order to estimate characteristics of the network. In [9] however, the authors illustrate that when applying a probing signal with frequency content close to a critical mode frequency, the oscillations become dangerously large. This indicates that the frequency content of the probing signal should be selected carefully and consequently, probing signal design is necessary. All methods presented in [6, 7, 8] do not take this into account, but rather probe the network with conventional (not optimized) probing signals. In this work, the probing signal is optimized.

Literature on probing signal design is found in [11, 12, 13, 14, 15]. In [11, 12, 13], the probing signal is pre-filtered such that it contains specific frequency content before being injected in the network. Although the frequency content of the probing signals is chosen more carefully, these existing methods do not optimize the probing signal so that the network's deviation from its nominal operating point and the probing signal's power content are minimized. This is however possible with the method presented in this work.

In [14], a multisine probing signal is considered and the phases of the multisine are in fact optimized to obtain a probing signal with the smallest amplitude, while having a user-defined power spectrum. Following linear system theory, it is not possible to enhance damping estimation by optimizing the phases of a multisine, but instead the power spectrum needs to be optimized. In contrast, the presented approach in this work explicitly enhances damping estimation via optimal probing design by optimizing the power spectrum of the probing signal.

In [15], the authors design the power spectrum of a multisine probing signal, (*i.e.*, the amplitudes of the different sinusoids) in such a way that a user-defined variance of the damping estimation is ensured, while minimizing the disturbance in the network due to probing. This work builds further on the work presented in [15] by enhancing it with the following contributions:

1. the introduction of a new discrete-time parameterization of a transfer function and covariance matrix containing, among others, damping coefficients,
2. the method is compared to a standard probing method [8],
3. the method is tested and simulated using a nonlinear power network model using both a "textbook" power grid model and a realistic power grid model and
4. in one test network, a high voltage direct current (HVDC) link based on voltage source converters is used to probe the network.

The remainder of this paper is organized as follows: Section 2 details the system identification method, which is used to find a damping estimation. During the experiment for system identification, the network is probed. Therefore, in Section 3, the probing signal design method is described. This paper is followed by Section 4 containing simulation results and is concluded in Section 5.

2. System Identification Method

The prediction error method [16, 17] is used as system identification technique. Here, measurements are used to estimate a model from which damping estimations are evaluated. In the prediction error method, the network's response $y(t)$[1], which for example can be the voltage angle difference between two buses, is approximated by $\hat{y}(t)$ that is composed of a superposition of two responses (ambient and probing), *i.e.*,

$$\hat{y}(t) = \underbrace{\hat{G}(z,\theta)u(t)}_{\text{probing}} + \underbrace{\hat{H}(z,\theta)e(t)}_{\text{ambient}}, \tag{1}$$

with causal and monic transfer function $\hat{H}(z,\theta)$ that is excited by white noise $e(t)$ (representing the random load changes) and causal transfer function $\hat{G}(z,\theta)$ that is excited (probed) by a probing signal $u(t)$. The latter is designed in this

[1] Appendix 5 contains a nomenclature.

work and can for example be active power. Furthermore, $t \in \mathbb{Z}$ represents the discrete-time, θ is the parameter vector to be estimated and $z \in \mathbb{C}$. Figure 1 depicts schematically the network as considered in the prediction error identification method.

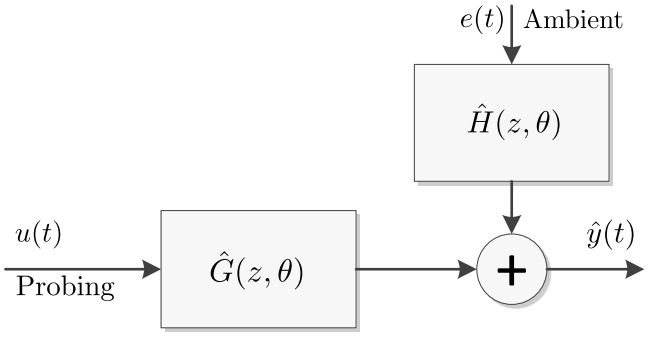

Figure 1: Power system representation as seen in the prediction error system identification method with probing signal $u(t)$ and measurement estimation $\hat{y}(t)$.

Both $\hat{H}(z,\theta), \hat{G}(z,\theta)$ are assumed to have the same denominators in this work. This allows to define the ARMAX model structure for $\hat{H}(z,\theta), \hat{G}(z,\theta)$:

$$\hat{y}(t) = \underbrace{\frac{b(z,\theta_b)\cdot z^{-n_k}}{a(z,\theta_a)}}_{\hat{G}(z,\theta)} u(t) + \underbrace{\frac{c(z,\theta_c)}{a(z,\theta_a)}}_{\hat{H}(z,\theta)} e(t), \qquad \theta = \begin{pmatrix} \theta_a \\ \theta_b \\ \theta_c \end{pmatrix} \in \mathbb{R}^{n_\theta}, \tag{2}$$

with polynomials:

$$\begin{aligned} a(z,\theta_a) &= z^{n_a} + \theta_1 z^{n_a-1} + \cdots + \theta_{n_a}, \\ b(z,\theta_b) &= \theta_{n_a+1} z^{n_b-1} + \theta_{n_a+2} z^{n_b-2} + \cdots + \theta_{n_a+n_b}, \\ c(z,\theta_c) &= z^{n_c} + \theta_{n_a+n_b+1} z^{n_c-1} + \cdots + \theta_{n_a+n_b+n_c}, \end{aligned} \tag{3}$$

and θ the unknown parameter vector that is found by the identification procedure. This has tuning parameters n_a, n_b, n_c, n_k and solves the following optimization problem:

$$\begin{aligned} \min_{\theta} \quad & \frac{1}{N}\sum_{t=1}^{N} \varepsilon(t,\theta)^2, \\ \text{subject to} \quad & \varepsilon(t,\theta) = \hat{H}(z,\theta)^{-1}\left(y(t) - \hat{G}(z,\theta)u(t)\right), \end{aligned} \tag{4}$$

with N the number of data points in the measurement that is seen as a bounded tuning parameter. Indeed, a larger N will result in a more precise estimation. However, the objective is to provide a new mode estimate every 10-15 minutes as done in practice [12] and consequently, N is bounded.

The probing signal design method employed in this work (see Section 3) demands for a parameterization of $\hat{G}(z,\theta), \hat{H}(z,\theta)$ in, among others, the damping coefficients (ζ_i) and their corresponding frequencies ($\omega_{n,i}$). Note that these are not the parameters defined in θ as found by the identification procedure. It is therefore necessary to re-parametrize the model in terms of $\zeta_i, \omega_{n,i}$. This new ARMAX model parameterization is presented in the following.

ARMAX model parameterization in $\omega_{n,i}$ and ζ_i

In order to define the desired ARMAX model parameterization, the poles of $\hat{G}(z,\theta)$ are firstly evaluated. These are assumed to be inside the unit circle and are found by solving $a(z,\theta_a) = 0$ (see (2)) for z. Let these poles be:

$$\aleph = \{z_1, z_2, \ldots, z_{n_r}, z_{n_r+1}, \bar{z}_{n_r+1}, \ldots, z_{n_r+n_i}, \bar{z}_{n_r+n_i}\}, \tag{5}$$

with $\bar{\bullet}$ the complex conjugate of the variable $\bullet$, n_r the number of real valued poles and n_i the number of complex pole pairs. Then define p as a subset of $\aleph$:

$$p = \{|z_1|, |z_2|, \ldots, |z_{n_r}|, z_{n_r+1}, z_{n_r+2}, \ldots, z_{n_r+n_i}\}. \tag{6}$$

The damping ratios and natural frequencies are evaluated as:

$$\zeta_i = \frac{\left|\mathrm{Re}\{\ln(p_i)\}\right|}{|\ln(p_i)|} \qquad \text{and} \qquad \omega_{n,i} = \frac{|\ln(p_i)|}{h}, \quad \forall p_i \neq 0, 1, \tag{7}$$

with h the sample period, $\mathrm{Re}\{\bullet\}$ the real part of the variable $\bullet$ and $\ln(\bullet)$ the natural logarithm function. If $p_i = \{0, 1\}$ then $\zeta_i = 1$. The following new parameterization of the polynomial $a(z,\theta_a)$ is now introduced:

$$\begin{aligned} a(z,\theta_\zeta) = &\prod_{i=1}^{n_i} \left(z^2 - 2e^{-\zeta_i \omega_{n,i} h} \cos(\omega_{n,i}\sqrt{1-\zeta_i^2}h) z + e^{-2\zeta_i \omega_{n,i} h} \right) \ldots \\ &\ldots \prod_{j=1}^{n_r} \left(z - \mathrm{sign}(z_j) e^{-\omega_{n,j}^r h} \right), \end{aligned} \tag{8}$$

with z_j the real valued pole location and $\omega_{n,j}^r$ its corresponding natural frequency. The natural frequency and damping coefficient that correspond to each complex pole pair are defined as $\omega_{n,i}$ and ζ_i, respectively. Then define:

$$\theta_\zeta = \begin{pmatrix} \zeta_1 & \dots & \zeta_{n_i} & \omega_{n,1} & \dots & \omega_{n,n_i} & \omega_{n,1}^r & \dots & \omega_{n,n_r}^r \end{pmatrix}^T, \tag{9}$$

with θ_ζ and θ_a having the same dimensions.

It should be clear that the polynomial $a(z, \theta_a)$ in (2) is equal to $a(z, \theta_\zeta)$ in (8), but only parameterized differently. In other words:

$$\hat{G}(z, \theta) = \hat{G}(z, \rho), \qquad \hat{H}(z, \theta) = \hat{H}(z, \rho), \tag{10}$$

with new parameter vector:

$$\rho = \begin{pmatrix} \theta_\zeta^T & \theta_b^T & \theta_c^T \end{pmatrix}^T. \tag{11}$$

The following steps are followed to evaluate $\hat{G}(z, \rho), \hat{H}(z, \rho)$:

1. Find $\hat{G}(z, \theta), \hat{H}(z, \theta)$ by solving (4).
2. Solve $a(z, \theta_a) = 0$ for z to find the poles $\aleph$ in (5).
3. Define p in (6) from $\aleph$.
4. Evaluate $\zeta_i, \omega_{n,i}$ using (7).
5. Evaluate the polynomial $a(z, \theta_\zeta)$ given in (8).

Listing 1: Steps to follow in order to define $\hat{G}(z, \rho), \hat{H}(z, \rho)$.

The newly parameterized $\hat{G}(z, \rho), \hat{H}(z, \rho)$ are then defined and used in the probing signal design method (see Section 3). This implies indeed that the presented method requires an initial $\hat{G}(z, \rho), \hat{H}(z, \rho)$, which are used to design the optimal probing signal. Section 4 details the procedure of obtaining such an initial $\hat{G}(z, \rho), \hat{H}(z, \rho)$.

This ends the proposed identification procedure's description. As state before, in order to perform system identification, the network needs be probed. This is carried out via the noise signal $e(t)$ and probing signal $u(t)$. The former cannot be chosen as it represents random load changes, though, the probing signal $u(t)$ must be designed. In the following section, such a probing design method is presented.

3. Probing Design Method

In order to perform system identification successfully, experimental conditions need to be designed. These conditions depend on the final objectives. In this work, these are to run experiments for system identification while minimizing the disturbances in the network and having a damping estimation with a user-defined variance. In order to achieve this goal, the probing signal's power spectrum is designed. In the following, the probing signal design method is detailed.

3.1. Optimization Problem Formulation

In order to find a probing signal's spectrum that minimizes the impact on the network while ensuring a user-defined upper bound on the damping estimation's variance, the following optimization problem is solved:

$$\begin{aligned} \min_{\Phi_u(\omega)} \quad & \left(\frac{c_1}{2\pi}\int_{-\pi}^{\pi}\Phi_u(\omega)\ \mathrm{d}\omega\right) + \left(\frac{c_2}{2\pi}\int_{-\pi}^{\pi}\Phi_y(\omega)\ \mathrm{d}\omega\right), \\ \text{subject to}: \quad & \text{variance}(\zeta_i) < \eta_i, \quad \text{for} \quad i = 1, 2, \ldots, n_i, \end{aligned} \tag{12}$$

where $\Phi_u(\omega)$ and $\Phi_y(\omega)$ are power spectra of the probing and output signal, respectively, and ω the continuous-time frequency. Furthermore, c_1 and c_2 are weighting factors and η_i is an upper bound on the damping coefficient's variance. Minimizing the first term in the objective results in a minimal effort of the actuators. Minimizing the second term results in a probing signal without unnecessary excitation power at the natural frequencies of low damped modes, because this may result in unwanted oscillations. A trade-off between these two terms must be made by tuning the weights c_1, c_2.

In this work, a multisine time-domain realization for the probing signal is adopted, *i.e.*:

$$u(t) = \sum_{r=1}^{M} A_r \cos(\omega_r t + \varphi_r), \tag{13}$$

where A_r, ω_r, φ_r are the magnitude, frequency and phase of the r^{th} sine component. The power spectrum of a multisine is defined as:

$$\Phi_u(\omega) = \frac{\pi}{2} \sum_{r=1}^{M} A_r^2 \Big(\delta(\omega - \omega_r) + \delta(\omega + \omega_r) \Big), \tag{14}$$

with $\delta(\bullet)$ the Dirac function. Furthermore, $A_r, \omega_r, \varphi_r, M$ are the user-defined magnitude, frequency and phase of the r^{th} sinusoidal component, respectively, and M the number of frequency components taken into account in the optimization problem (12). Note that in [14], the authors find φ_r (see (13)). The framework used in this work determines the amplitudes A_r in an optimal way whereas φ_r is chosen randomly and a grid is defined for ω_r. Due to the newly developed parameterization, the optimization problem defined in (12) is rewritten as:

$$\begin{aligned} \min_{A_r^2 (r=1,2,\ldots,M)} \quad & \frac{c_1}{2} \sum_{r=1}^{M} A_r^2 + \frac{c_2}{2} \sum_{r=1}^{M} A_r^2 \big| \hat{G}(\omega_r, \rho) \big|^2, \\ \text{subject to} \quad & \text{variance}(\zeta_i) < \eta_i, \quad \text{for} \quad i = 1, 2, \ldots, n_i, \\ & A_r^2 \geqslant 0, \qquad\qquad \text{for} \quad r = 1, 2, \ldots, M. \end{aligned} \tag{15}$$

The additional constraints $A_r^2 \geqslant 0$ are to ensure positivity for the probing signal's power (see (14)). Next, the constraints variance$(\zeta_i) < \eta_i$ are rewritten to a linear matrix inequality such that a convex optimization problem is obtained. For this, define the covariance matrix of the parameter vector ρ as $P_\rho = \text{variance}(\rho)$. Note that the variance of each damping coefficient is placed somewhere on its diagonal. Consequently, the constraint variance$(\zeta_i) < \eta_i$ is written as $e_i^T P_\rho e_i < \eta_i$, with i the damping coefficient's index and e_i the unity vector whose i^{th} element is equal to one. Then, by using the Schur complement, the constraint $e_i^T P_\rho e_i < \eta_i$ is written as an linear matrix inequality such that (15) becomes:

$$\begin{aligned} \min_{A_r^2 (r=1,2,\ldots,M)} \quad & \frac{c_1}{2} \sum_{r=1}^{M} A_r^2 + \frac{c_2}{2} \sum_{r=1}^{M} A_r^2 \big| \hat{G}(\omega_r, \rho) \big|^2, \\ \text{subject to} \quad & \begin{pmatrix} \eta_i & e_i^T \\ e_i & P_\rho^{-1} \end{pmatrix} > 0, \quad \text{for} \quad i = 1, 2, \ldots, n_i, \\ & A_r^2 \geqslant 0, \qquad\qquad \text{for} \quad r = 1, 2, \ldots, M. \end{aligned} \tag{16}$$

As shown in [17], the inverse of the covariance matrix P_ρ can be approximated by a first order approximation:

$$P_\rho^{-1} = \Big(\text{variance}(\rho)\Big)^{-1} = \frac{N}{2\pi}\left[\left(\frac{1}{\sigma_e^2}\int_{-\pi}^{\pi} F_u(\omega,\rho)F_u^*(\omega,\rho)\Phi_u(\omega)\ \mathrm{d}\omega\right) + \left(\int_{-\pi}^{\pi} F_e(\omega,\rho)F_e^*(\omega,\rho)\ \mathrm{d}\omega\right)\right],$$

with

- σ_e an estimation of the standard deviation of $e(t)$, and
- functions $F_u(\omega,\rho), F_e(\omega,\rho)$ defined as:

$$F_u(\omega,\rho) = \hat{H}(\omega,\rho)^{-1}\frac{\partial \hat{G}(\omega,\rho)}{\partial \rho} \quad \text{and} \quad F_e(\omega,\rho) = \hat{H}(\omega,\rho)^{-1}\frac{\partial \hat{H}(\omega,\rho)}{\partial \rho}.$$

Analytical expression for $\partial\hat{G}/\partial\rho$ and $\partial\hat{H}/\partial\rho$ are found in Appendix A. Due to the multisine parametrization of the probing signal, P_ρ^{-1} is evaluated as [17]:

$$P_\rho^{-1} = N\left[\left(\frac{1}{2\sigma_e^2}\sum_{r=1}^{M}\mathrm{Re}\{F_u(\omega_r,\rho)F_u^*(\omega_r,\rho)\}A_r^2\right) + \left(CXC^T + DD^T\right)\right], \quad (17)$$

with X the solution to the Lyapunov equation: $AXA^T + BB^T = X$ and the matrices A, B, C, D from the minimal state-space realization of $F_e(\omega,\rho)$. From (17), it is to be noted that more power in the probing signal (larger A_r^2) and more data points in the measurement (larger N) will result in a smaller variance of the parameter vector ρ and thus also ζ_i. However, as stated before, the objective is also to minimize the disturbance in the network due to probing. The optimization problem formulated in (16) takes this into account.

An important question that needs to be addressed is the actual instant at which probing is to be applied. For example, when damping values are close to a certain lower bound for which oscillations in the network occur, probing is invaluable in order to provide an accurate damping estimation. This is a challenging problem and a research subject by itself [12] and it will be addressed in future research. Furthermore, in this work it is assumed that the moment of probing is known as this is also current practice [8]. Furthermore, a choice

must be made for probing and measurement locations in the network. For example, the probing signal can be the reactive power injected at a bus where a power electronic device is placed. A measurement can be the phase angle or frequency difference between two buses in the network where phasor measurement units are placed. One criteria for these choices is that the probing signal should have sufficient impact on the measurement's observability of the mode of interest. In other words, the measurement should be sufficiently enriched by the probing signal. There are methods that allow to find probing and measurement locations [18]. In this work, however, these were chosen empirically such that an identified and validated model is obtained. A last remark on the proposed framework is that actuation limitations are not taken into account (an ideal actuator is assumed). In practice, however, an actuator is not ideal due to delays, saturation and filtering. Nevertheless, the frequency content of the probing signal is crucial for the proposed methodology. The assumption is therefore that the actuator generates probing signals that contain all frequencies ω_r for $r = 1, \ldots, M$ (see (13)).

Note that the covariance matrix's expression P_ρ, which is used in (16), requires an initial estimate of the parameter vector ρ. In other words, it requires an initial identified model. The following section describes how this model is obtained and when the optimized probing signal is applied so that accurate damping estimations are obtained.

4. Simulation Results

This section discusses the used software, two applied simulation procedures for estimating the network's damping and how the outcome of these procedures is compared. Then, the simulation results are presented and discussed for two different power system non-linear simulation models.

4.1. Software

The employed programs are Matlab (for system identification) and Modelica tool Dymola in combination with the OpenIPSL library [19] (for power system

modeling). The library was built to model nonlinear power system networks using the phasor (*i.e.*, positive-sequence) modeling approach. All developed Dymola models and also the Matlab scripts that solve the system identification problem and the optimal probing signal selection are placed on a Github repository [20].

4.2. Simulation Procedures

In order to demonstrate the proposed method's effectiveness, two different simulation procedures are discussed below and schematically depicted in Fig. 2. The first (base) procedure follows a similar approach as presented in [8], while the second (optimal) procedure follows the approach as presented in this work. The two approaches are later compared, but first detailed as follows:

1) Base Procedure

The following steps are followed in the base procedure:

1. Manually define a probing signal $u_{\text{base}}(t)$ with linearly spaced $\omega_r \in [0.1\ 3]$ (Hz) with $M = 30$ (see (13)).
2. Perform a system identification experiment taking $t_2 - t_0$ seconds and collect measurement $y(t)$.
3. Follow the steps listed in Listing 1 to evaluate $\hat{G}_{\text{base}}(z, \rho)$, $\hat{H}_{\text{base}}(z, \rho)$.
4. Evaluate the variance $P_{\rho,\text{base}}$ using (17).

Listing 2: Steps to follow in the base procedure.

The variance $P_{\rho,\text{base}}$ is used in the optimal procedure. In the base procedure, the tuning variables n_a, n_b, n_c, n_k, time-window of probing ($t_2 - t_0$ seconds) and probing signal $u_{\text{base}}(t)$ are chosen manually such that an identified (and validated) model is obtained. Note that the time-window of probing in the base procedure is not found by solving an optimization problem, similarly to current practice [8]. Also note that the chosen probing signal $u_{\text{base}}(t)$ contains empirically found amplitudes as done in [8], which is in contrast to the optimal procure that is described next.

2) Optimal Procedure

The optimal procedure contains two experiments and its objective is to obtain an equivalent variance on the damping estimation as obtained during the base experiment ($P_{\rho,\text{base}}$), though while minimizing the disturbance in the network (less power in the probing and measurement signals). The following steps are followed in the optimal procedure:

1. Manually define a probing signal $u_{\text{base}}(t)$ with linearly spaced $\omega_r \in [0.1\ 3]$ (Hz) with $M = 30$ (see (13)).
2. Perform a system identification experiment taking $t_1 - t_0$ seconds with $t_1 = t_2/2$ and collect measurement $y(t)$.
3. Follow the steps listed in Listing 1 to evaluate $\hat{G}_1(z,\rho)$, $\hat{H}_1(z,\rho)$.
4. Evaluate the variance $P_{\rho,1}$ using (17).
5. Solve the proposed probing design method given in (16) with

$$\eta_i^{-1} = \left(e_i^T P_{\rho,\text{base}} e_i\right)^{-1} - \left(e_i^T P_{\rho,1} e_i\right)^{-1}, \tag{18}$$

   for $i = 1, \ldots, n_i$.
6. Define the optimized probing signal $u_{\text{opt}}(t)$.
7. Perform a system identification experiment taking $t_2 - t_1$ seconds by probing with $u_{\text{opt}}(t)$ and collect measurement $y(t)$.
8. Follow the steps listed in Listing 1 to evaluate $\hat{G}_2(z,\rho)$, $\hat{H}_2(z,\rho)$.
9. Evaluate $\hat{G}_{\text{opt}}(z,\theta)$ and $\hat{G}_{\text{opt}}(z,\rho)$ using the steps given in Appendix Appendix B and Listing 1.

Listing 3: Steps to follow in the optimal procedure.

It should be clear that the upper bound η_i in the fifth step is the user-defined design constraint. It is set to a value which ensures that the optimal procedure combining the manually chosen (during first $t_1 - t_0$ seconds) and the optimized (during last $t_2 - t_1$ seconds) probing signal yield an estimate of the damping whose variance is smaller or equal to the variance of the damping's estimate in the base procedure.

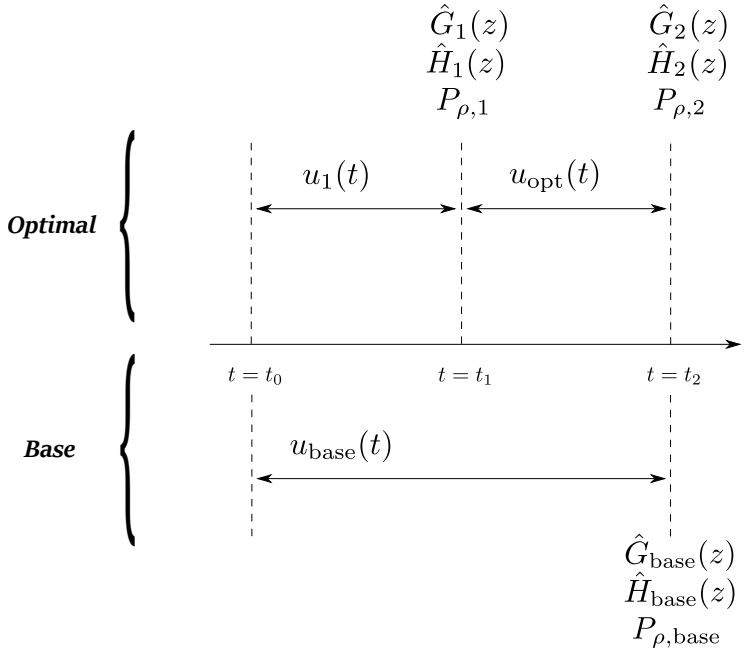

Figure 2: Schematic representation of the base procedure, which is similar to [14] and the proposed optimal procedure.

Quality measures are introduced in the following section in order to compare the two procedures and to ensure that the identified models are valid.

4.3. Quality Measures

In order to validate the identified model and proposed framework, the following quality measures are introduced:

i) The Bode diagrams of the identified models (both base and optimal procedure) are compared with those of the nonlinear power system model, linearized by using [21].

ii) The sample mean and the sample variance of the estimates in the base and the optimal procedure are evaluated by means of Monte Carlo simulations to verify that the damping estimate's accuracy in the optimal procedure is larger or equal to the one in the base procedure.

Quality measure i) ensures that identified models are valid. This quality measure is used to tune the identification parameters n_a, n_b, n_c, n_k, N, *i.e.*, it is used to find a proper model structure (see (2)) and time-window $(t_2 - t_0)$. For quality measure ii), the sample variance is defined as:

$$\hat{P}_{\zeta_i,\bullet} = \frac{1}{L-1} \sum_{j=1}^{L} |\zeta_{i,j} - \overline{\zeta}_i| \quad \text{with} \quad \overline{\zeta}_i = \frac{1}{L} \sum_{j=1}^{L} \zeta_{i,j}, \tag{19}$$

with $\zeta_{i,j}$ estimation j of ζ_i, L the total number of estimations and $\overline{\zeta}_i$ its sample mean.

4.4. Optimal Probing Design Simulation Results

4.4.1. Test network 1: Kundur with an embedded HVDC link

Figure 3 depicts schematically a representation of the modified Kundur network.

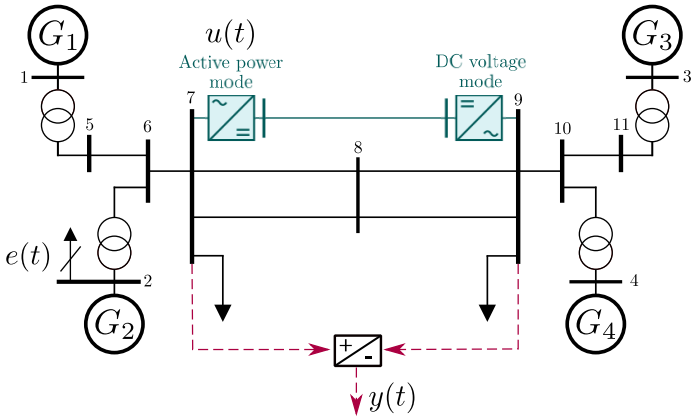

Figure 3: Schematic representation of the Kundur network with an embedded HVDC link.

The probing signal $u(t)$ is the active power through the HVDC link and the measurement $y(t)$ is the phase angle difference between bus 7 and 9. The random load changes are represented by the noise $e(t)$ with standard deviation $5 \cdot 10^{-4}$ and injected in bus 2. This network's minimum under-damped inter-area mode is located at $\omega_{\text{true}} = 0.63$ Hz with a damping coefficient of $\zeta_{\text{true}} = 0.015$ and contains also two other low-damped local modes around 1.1 and 1.3 Hz.

These values are calculated from the linearized Dymola network using [21] and used only for comparison.

1) Base Procedure Results: Kundur with an embedded HVDC link

Table 1 provides the parameters that are used during the base procedure (see Listing 2). The parameters n_a, n_b, n_c, n_k, N are tuned such that quality measure i) is ensured (the Bode diagram is shown later).

Table 1: Parameters that are used in the Kundur network with HVDC link.

Parameter	t_0	t_1	t_2	N	h	n_a	n_b	n_c	n_k	M	ω_r	A_r
Value	0	60	120	2400	0.05	4	4	2	1	30	[0.1 3] (Hz)	0.03

2) Optimal Procedure Results: Kundur with an embedded HVDC link

The steps listed in Listing 3 are followed for two different pairs of weighting factors c_i (see (16)).

a) $c_1 = 1, c_2 = 0$. The optimized multisine amplitudes that are found using (16) are depicted in Fig. 4. As shown in that figure, they are centered around the local low-damped modes located at 1.3 Hz and (mostly) around the inter-area mode (vertical black dashed line). This is explained by the fact that the optimization problem in (16) minimizes only the power in the probing signal when $c_2 = 0$. Therefore, in order to obtain the required variance on the damping coefficient, it is more efficient to mostly probe around the inter-area mode. This is however undesirable as explained before and can be improved by introducing $c_2 > 0$ as is shown later.

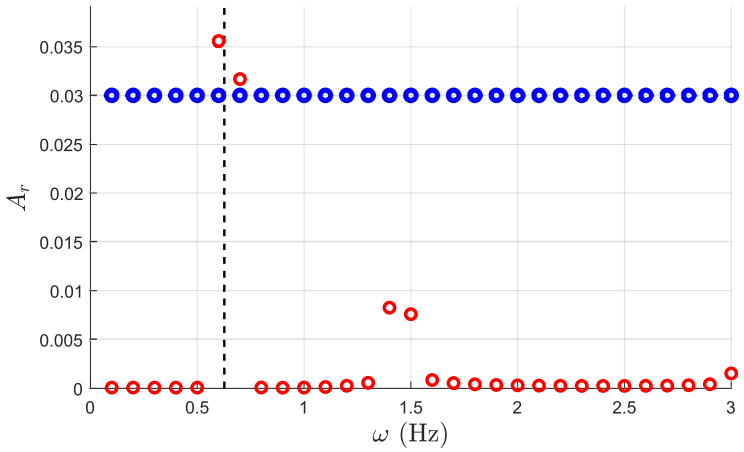

Figure 4: The amplitudes A_r from the base procedure (blue), and optimized ones (red) with $c_1 = 1, c_2 = 0$. The vertical dashed line indicates the frequency of the true inter-area mode.

The time-domain results are shown in Fig. 5. Here, the first subplot depicts the measurement $y(t)$ (blue) and the simulation output from the identified model $\hat{y}(t)$ (red). The second subplot shows the probing signal $u(t)$. Note that there is a difference in probing between $t_0 = 0$ until $t_1 = 60$ (manual probing) and $t_1 = 60$ until $t_2 = 120$ (optimal probing).

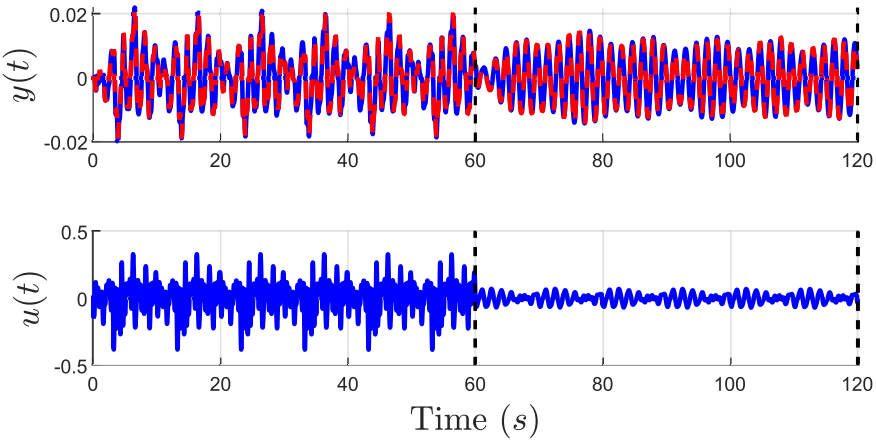

Figure 5: Identification results obtained following the optimal procedure with $c_1 = 1, c_2 = 0$. The probing signal $u(t)$ has MW as units and its value is plotted around an equilibrium value.

b) $c_1 = 1/2, c_2 = 2500$. The optimized multisine amplitudes that are found using (16) are depicted in Fig. 6.

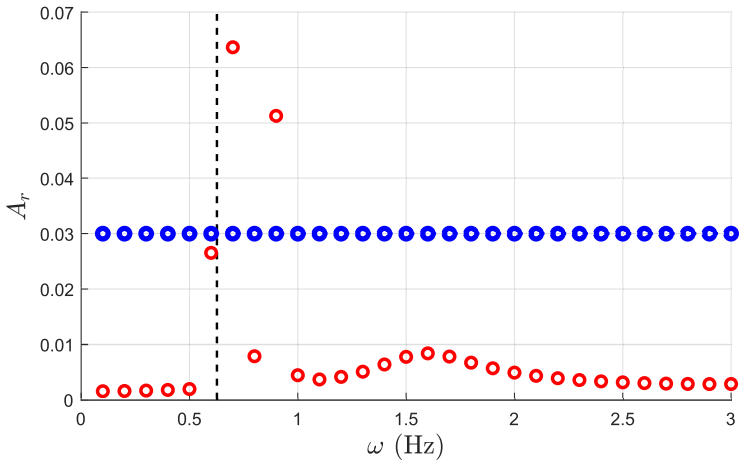

Figure 6: The amplitudes A_r from the base procedure (blue), and optimized ones (red) with $c_1 = 1/2, c_2 = 2500$. The vertical dashed line indicates the frequency of the true inter-area mode.

Observe that, with respect to the previously found amplitudes (Fig. 4), the frequency that is closest to the inter-area mode is less excited, which is desired as explained previously. This is due to setting $c_2 > 0$ in (16) so that also the output is minimized. Consequently, probing the network close to its inter-area mode is penalized. On the other hand, around the inter-area mode, the amplitudes are increased in order to ensure the demanded variance on the damping coefficients. The time-domain results are shown in Fig. 7.

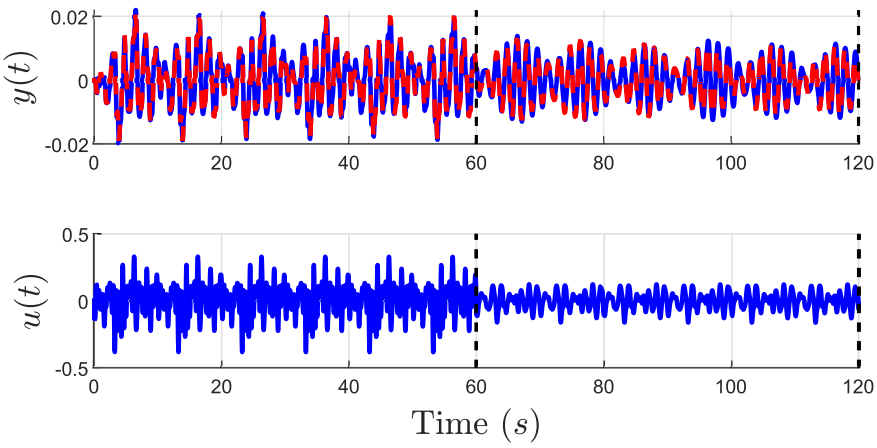

Figure 7: Identification results obtained following the optimal procedure with $c_1 = 1/2, c_2 = 2500$. The probing signal $u(t)$ has MW as units and its value is plotted around an equilibrium value.

3) Comparison Base and Optimal: Kundur with an embedded HVDC link

Figure 8 depicts the Bode magnitude plots of the nonlinear power system model after being linearized in Dymola, and of all three identified models. One model obtained during the base procedure ($\hat{G}_{\text{base}}$) and one for each optimal procedure ($\hat{G}_{\text{opt}_1}, \hat{G}_{\text{opt}_2}$). It can be observed that the dominant characteristics of interest for this work are captured with the identified models, but that the local modes above 1 Hz are not perfectly approximated. This is due to the fact that the identified models contain 4 poles with respect to the 46 poles in the linearized power system model. In any case, for the proposed damping estimation method, it is important to estimate accurately the lowest damping coefficient, which is reflected in the peak around 0.63 Hz in the Bode magnitude plot and not other relatively high valued coefficients. The identified models estimate this peak sufficiently well.

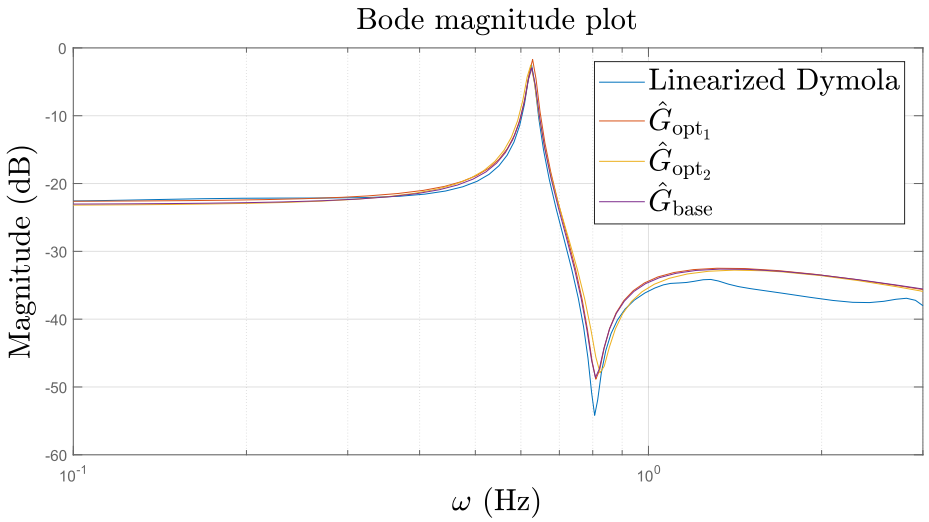

Figure 8: Bode magnitude plot of the three estimated models and the linearized nonlinear network.

In order to verify quality measure *ii*), for all three cases, 100 nonlinear time-domain simulations are conducted and damping estimations are obtained. The estimation's sample means and variances (19) are evaluated. The results for the lowest damping coefficient are depicted in Table 2. This table also shows the average normalized power in the probing signal and measurement.

Table 2: Simulation results for the Kundur network with an embedded HVDC link.

	sample mean	sample variance	normalized probing signal power	normalized measurement power
Base procedure	0.018	$4.6 \cdot 10^{-7}$	1	1
Optimal procedure 1	0.016	$18 \cdot 10^{-7}$	0.1	0.85
Optimal procedure 2	0.017	$9.9 \cdot 10^{-7}$	0.3	0.6

Recall that the lowest damping value, obtained when linearizing the nonlinear power system model, is 0.015. Even though this is not taken into account in our procedure, we observe a small bias in the three identification procedures. Among other reasons, this bias can be explained by the use of a lower order model structure to identify the system [17]. Due to the presence of the bias,

the accuracy of a given estimate can be best evaluated using the MSE which is equal to the sum of the variance and of the squared bias. The (sample) MSE for the estimate obtained with the base procedure is thus here equal to $9.46 \cdot 10^{-6}$ while this MSE is respectively equal to $2.8 \cdot 10^{-6}$ and $4.99 \cdot 10^{-6}$ in the two optimal procedures. We thus indeed observe that the accuracy obtained in the two optimal procedures are larger or equal than the one in the base procedure. It should also be noted that the bias is relatively low for practical purpose and it is consistent with other similar research [22].

The probing signal's and measurement average power are in the first optimal procedure approximately 90% and 15% lower, respectively, compared to the base procedure. This is in the second optimal procedure 70% and 40% lower, respectively. Comparing the two optimal procedures, it can be observed that in the second one, there is less average power in the measurement. This is as expected since $c_2 = 2500$ in (16) is introduced, which penalizes the measurement's deviation from its nominal value. However, in order to still ensure the demanded variance in the second optimal procedure, the average power in the probing signal increased with respect to the first optimal procedure. This clearly illustrates the trade-off between average power in the probing signal and measurement, which is regulated by the weights c_1, c_2 in (16).

4.4.2. Test network 2: Nordic 44

The second case study is the Nordic 44-bus test network [23]. Via a Voltage Source Converter working in STATCOM mode (modeled as in [24]), reactive power $u(t)$ is injected at bus 3020 and the measurement $y(t)$ is chosen to be the angle difference between bus 5601 and bus 7010. The random load changes that are modeled by $e(t)$ with a standard deviation 0.02, are injected in bus 7020. The Nordic 44 has in total 374 under damped modes. The lowest is at $\omega_{\text{true}} = 0.4$ Hz with a damping coefficient of $\zeta_{\text{true}} = 0.01$. The second lowest is at 0.95 Hz having a value of 0.07. These two are the most dominant inter-area modes. The interested reader is referred to [23, 24] for a schematic representation of the Nordic 44-bus test network.

1) Base Procedure Results: Nordic 44

Table 3 provides the parameters that are used during the base procedure (see Listing 2). The parameters n_a, n_b, n_c, n_k, N are tuned such that quality measure i) is ensured (the Bode diagram is shown later).

Table 3: Parameters that are used in the Nordic 44 network.

Parameter	t_0	t_1	t_2	N	h	n_a	n_b	n_c	n_k	M	ω_r	A_r
Value	0	450	900	1200	0.1	6	3	3	0	30	[0.1 3] (Hz)	0.01

2) Optimal Procedure Results: Nordic 44

The steps listed in Listing 3 are followed for two different pairs of weighting factors c_i (see (16)).

a) $c_1 = 1, c_2 = 0$. The optimized multisine amplitudes that are found using (16) are depicted in Fig. 9. Observe in this figure again that the optimal probing signal is centering its energy around the (in this test case) two most dominant inter-area modes. The frequencies that belong to these modes are illustrated by the black vertical dashed lines. This is due to the fact that $c_2 = 0$ for this optimal experiment and thus, the objective is to minimize the probing signal's energy and not the output power's energy. This steers the optimal probing signal's energy around the most dominant inter-area modes.

A zoom-in of the time-domain results is shown in Fig. 10. Here, the first subplot depicts the measurement $y(t)$ (blue) and the simulation output from the identified model $\hat{y}(t)$ (red). The second subplot shows the probing signal $u(t)$. Note that there is a difference in probing between $t_0 = 0$ until $t_1 = 450$ (manual probing) and $t_1 = 450$ until $t_2 = 900$ (optimal probing).

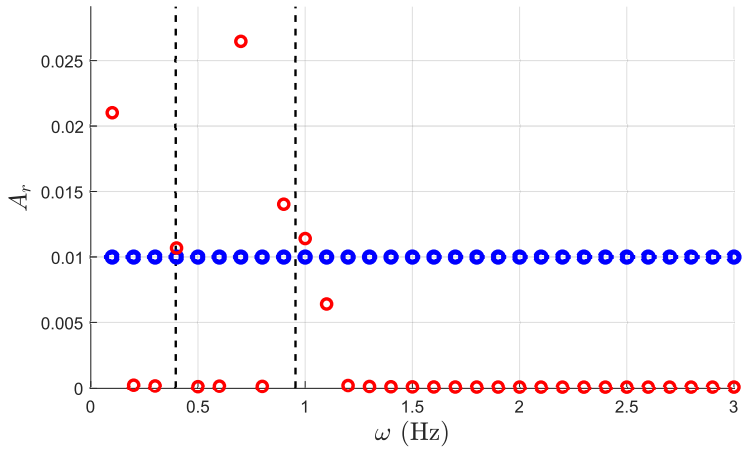

Figure 9: The amplitudes A_r from the base procedure (blue), and optimized ones (red) with $c_1 = 1, c_2 = 0$. The vertical dashed lines indicate the true most dominant inter-area modes' frequency.

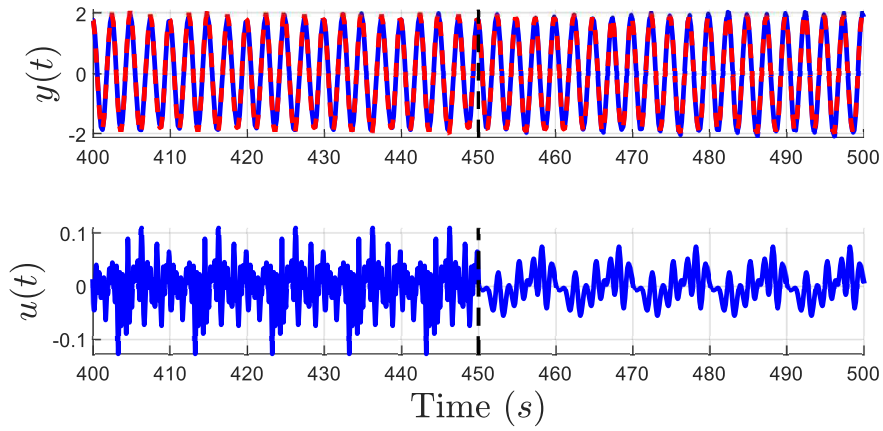

Figure 10: Zoom-in of the identification results obtained following the optimal procedure with $c_1 = 1, c_2 = 0$. The probing signal $u(t)$ is plotted in percentages of its nominal value (*i.e.*, 0.1 means a 10% deviation of its nominal value).

b) $c_1 = 3/4, c_2 = 1/4$. The optimized multisine amplitudes that are found using (16) are depicted in Fig. 11.

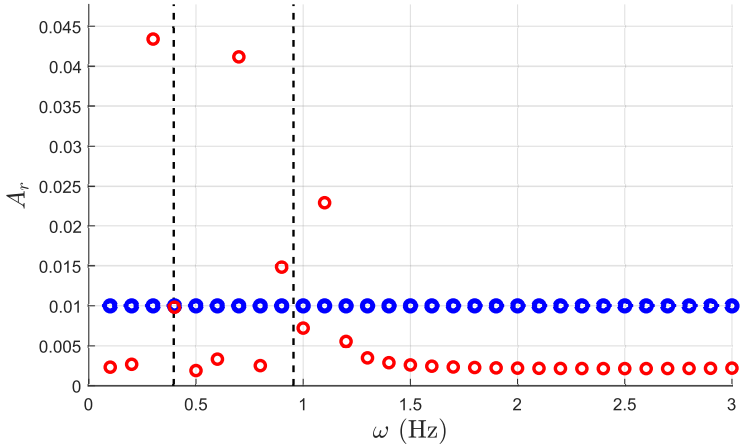

Figure 11: The amplitudes A_r from the base procedure (blue), and optimized ones (red) with $c_1 = 3/4, c_2 = 1/4$. The vertical dashed lines indicate the true most dominant inter-area modes' frequency.

Observe in Fig. 11 that the optimal probing signal's power around the two frequencies, which belong to the two most dominant inter-area modes, is reduced with respect to the previous optimal experiment. However, in order to ensure the demanded accuracy of the damping estimation, the optimal amplitudes of other frequency components in the probing signal are increased. This is again due to introducing $c_2 > 0$. A zoom-in of the time-domain results is shown in Fig. 12.

3) Comparison Base and Optimal: Nordic 44

Figure 13 depicts the Bode magnitude plots of the nonlinear power system model after being linearized in Dymola, and of all three identified models. One model obtained during the base procedure ($\hat{G}_{\text{base}}$) and one for each optimal procedure ($\hat{G}_{\text{opt}_1}, \hat{G}_{\text{opt}_2}$). It can be observed that the dominant characteristics are again captured with the identified models containing the modes with lowest damping at 0.4 Hz and 0.95 Hz. The local mode around 0.5 Hz is not approximated, which is due to the fact that the identified models contain 6 poles with

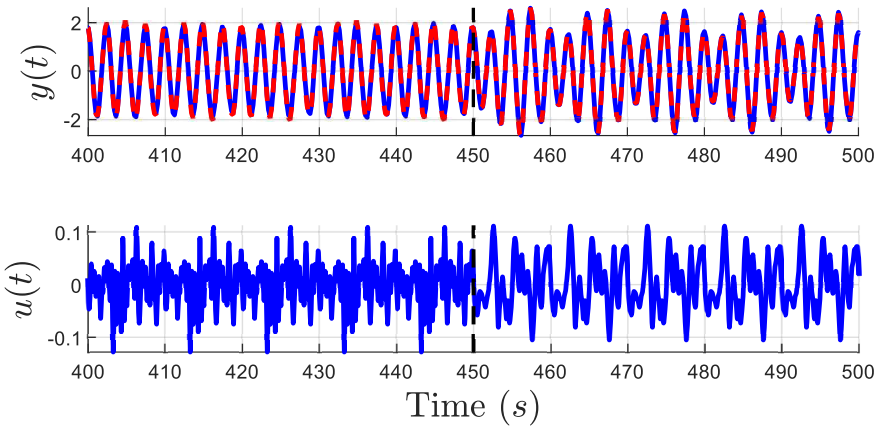

Figure 12: Zoom-in of the identification results obtained following the optimal procedure with $c_1 = 3/4, c_2 = 1/4$. The probing signal $u(t)$ is plotted in percentages of its nominal value (*i.e.*, 0.1 means a 10% deviation of its nominal value).

respect to the 1013 poles in the linearized Dymola model. As in the previous example, the identified models contain the important information for the current application, which is damping estimation.

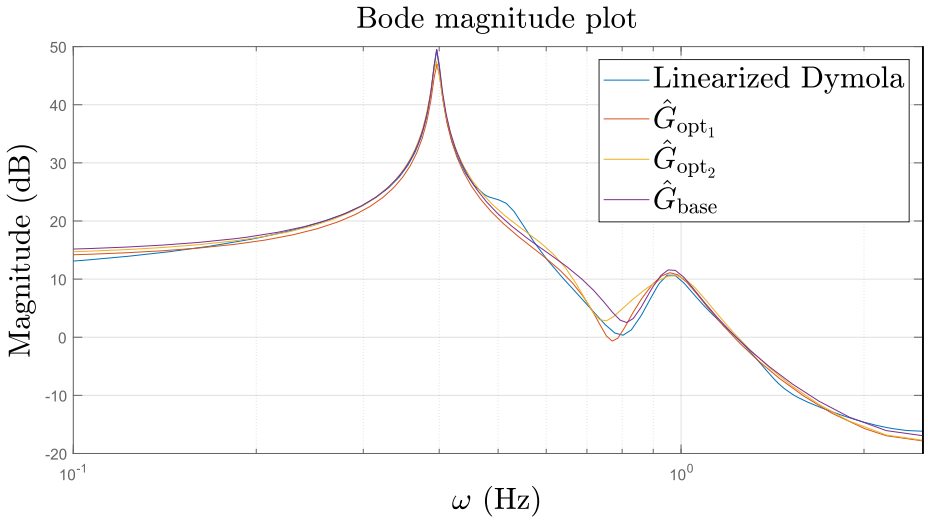

Figure 13: Bode magnitude plot of the three estimated models and the linearized nonlinear network.

In order to verify quality measure *ii*), for all three cases, 10 nonlinear time-domain simulations are conducted and damping estimations are obtained. The estimation's sample means and variances (19) are evaluated. Only 10 simulations are conducted per procedure because each simulation requires 48 hours to be completed. Although the results are not fully statistically significant, they still give an insight in the proposed method's validity. The results for the lowest damped damping coefficient are depicted in Table 4. This table also shows the average normalized power in the probing signal and measurement.

Table 4: Simulation results for the Nordic 44.

	sample mean	sample variance	normalized probing signal power	normalized measurement power
Base procedure	0.013	$1.7 \cdot 10^{-8}$	1	1
Optimal procedure 1	0.014	$4.0 \cdot 10^{-8}$	0.82	1.17
Optimal procedure 2	0.012	$34 \cdot 10^{-8}$	1.5	0.92

Recall that the lowest damping value from the linearized Dymola model is 0.01. We here also observe a bias and we therefore also compute the sample MSE to evaluate the accuracy of the estimates obtained in the three identification procedures: MSE= $9.017 \cdot 10^{-6}$ for the base procedure, MSE= $16.04 \cdot 10^{-6}$ for the first optimal procedure and MSE= $4.34 \cdot 10^{-6}$ for the second optimal procedure. We observe that this MSE is small for the three procedures, but, contrary to what would be expected, the MSE in the first optimal procedure is larger than the one in the base procedure. This discrepancy could perhaps be explained by the relatively low number of Monte-Carlo simulations.

The probing signal's and measurement average power are in the first optimal procedure approximately 18% lower and 17% higher, respectively, compared to the base procedure. These results coincide with the fact that the focus in this optimal experiment is on the minimization of the probing signal's power ($c_2 = 0$) and not on the measurement's power. For the second optimal procedure, the probing signal's and measurement average power are approximately 50% higher and 8% lower, respectively, compared to the base procedure. This results again

clearly indicates that the presented optimal probing design framework allows the user find a trade-off between probing signal and measurement power content during the system identification experiment for damping coefficient estimation.

5. Conclusions

Inter-area mode estimation has proven to be one of the key applications in PMU-based wide-area monitoring systems for power system operation. For example, a damping estimate below a certain threshold can serve to indicate when corrective control actions needs to be taken. However, taking such action requires a high degree of confidence that the damping estimates are accurate, which translates into a low variance requirement on the estimates. This is a challenge in ambient data-based estimators because the excitation of a particular mode can be low and consequently resulting in damping estimates with unacceptable variance. While probing methods have been applied in the past to address this issue, they do not provide any means to constraint on the amount of perturbation that the power network experiences due to the probing signal injection, which is undesirable.

To address these challenges, this work presented a method that provides damping estimations with guaranteed accuracy, while minimizing the perturbations in the network. The method combines system identification and optimal probing signal design. An identified model is used to evaluate an optimal probing signal, which is then applied to find the accurate damping estimation. The framework presented in this paper allows the probing signal designer to make a trade-off between the power in the probing signal and measurement for an ensured estimation accuracy. The proposed framework is demonstrated through two simulation examples. One relatively small example with an embedded HVDC link and one realistic grid model called the Nordic 44. It has been shown that by utilizing an advanced probing design method, accurate damping coefficient estimations are provided while simultaneously minimizing the network's perturbation. A comparison with a standard probing design method

shows that the proposed method causes less perturbations in the network, while having an equivalent estimation accuracy.

Even though the model parameters that are estimated by the proposed method are random variables by itself (they are uncertain), the method does not take uncertain network parameters into account. This is an interesting avenue for future work. This also hold for the application of the proposed method on a power system model with power hardware in the loop of an HVDC controller such that the method can be tested even better.

Nomenclature

System Identification

t, z	Discrete-time and complex variable, respectively
$u(t), e(t)$	Probing signal and white noise (random load changes), respectively
$y(t), \hat{y}(t)$	Network's response (measurement) and its estimation, respectively
$\hat{G}(z,\theta), \hat{H}(z,\theta)$	Identified model parameterized in θ
θ	Parameter vector found by the identification method
$\hat{G}(z,\rho), \hat{H}(z,\rho)$	Identified model parameterized in ρ
ρ	Parameter vector with, among others, $\zeta_i, \omega_{n,i}$
$\zeta_i, \omega_{n,i}$	Estimated damping coefficient i and its corresponding natural frequency
n_a, n_b, n_c, n_k	Tuning variables of the identification procedure
N, h	Number of data points in, and sample period of the data used for identification
n_i, n_r	Number of complex pole pairs and real poles, respectively, in the identified model

Probing Signal Design

ω	Continuous-time frequency
Φ_u, Φ_y	Power spectrum probing signal and measurement, respectively
$A_r, \omega_r, \varphi_r, M$	Parameters of the probing signal (multisine)
c_1, c_2	Tuning variables of the optimal probing design procedure
η_i	Upper bound on variance(ζ_i)
P_ρ	Covariance matrix of the parameter ρ
$\hat{P}_\rho$	Sample covariance matrix of the parameter ρ

Simulation Results

$\hat{y}(t)$	Output of the identified model (estimation of $y(t)$)
$\zeta_{\min}, \omega_{\min}$	Lowest estimated damping coefficient and its corresponding natural frequency
$\zeta_{\text{true}}, \omega_{\text{true}}$	Lowest true damping coefficient and its corresponding natural frequency

Appendix A.

Recall that the parameter vector was defined as: $\rho = \begin{pmatrix}\theta_\zeta^T & \theta_b^T & \theta_c^T\end{pmatrix}^T$, with

$$\theta_\zeta = \begin{pmatrix}\omega_{n,1}^r & \dots & \omega_{n,n_r}^r & \omega_{n,1} & \zeta_1 & \dots & \omega_{n,n_i} & \zeta_{n_i}\end{pmatrix}^T,$$
$$\theta_b = \begin{pmatrix}\theta_{n_a+1} & \dots & \theta_{n_a+n_b}\end{pmatrix}^T, \quad \theta_b = \begin{pmatrix}\theta_{n_a+n_b+1} & \dots & \theta_{n_a+n_b+n_c}\end{pmatrix}^T.$$

The transfer functions defined in (2) are re-written as:

$$\hat{G}(z,\rho) = m(z)\underbrace{\begin{pmatrix}0_{n_a-n_b}\\ \theta_{n_a+1}\\ \vdots\\ \theta_{n_a+n_b}\end{pmatrix}}_{B_g(\theta_b)} a(z,\theta_\zeta)^{-1}z^{-n_k}, \qquad \hat{H}(z,\rho) = m(z)\underbrace{\begin{pmatrix}1\\ \theta_{n_a+n_b+1}\\ \vdots\\ \theta_{n_a+n_b+n_c}\end{pmatrix}}_{B_h(\theta_c)} a(z,\theta_\zeta)^{-1},$$

with

$$m(z) = \begin{pmatrix}z^{n_a} & z^{n_a-1} & \dots & z & 1\end{pmatrix} \in \mathbb{R}^{n_a+1},$$

and

$$a(z,\theta_\zeta) = \prod_{i=1}^{n_i}\left(z^2 - 2e^{-\zeta_i\omega_{n,i}h}\cos(\omega_{n,i}\sqrt{1-\zeta_i^2}h)z + e^{-2\zeta_i\omega_{n,i}h}\right)\prod_{j=1}^{n_r}\left(z - \text{sign}(z_j)e^{-\omega_{n,j}^r h}\right).$$

The analytical expressions of the partial derivatives are defined as:

$$\frac{\partial\hat{G}(z,\rho)}{\partial\rho} = \begin{pmatrix}\frac{\partial\hat{G}(z,\rho)}{\partial\omega_{n,1}}\\ \vdots\\ \frac{\partial\hat{G}(z,\rho)}{\partial\omega_{n,n_r}}\\ \frac{\partial\hat{G}(z,\rho)}{\partial\omega_{n,n_r+1}}\\ \frac{\partial\hat{G}(z,\rho)}{\partial\zeta_{n_r+1}}\\ \vdots\\ \frac{\partial\hat{G}(z,\rho)}{\partial\omega_{n,n_r+n_i}}\\ \frac{\partial\hat{G}(z,\rho)}{\partial\zeta_{n_r+n_i}}\\ \hline \frac{\partial\hat{G}(z,\rho)}{\partial\rho_{n_a+1}}\\ \frac{\partial\hat{G}(z,\rho)}{\partial\rho_{n_a+2}}\\ \vdots\\ \frac{\partial\hat{G}(z,\rho)}{\partial\rho_{n_a+n_b}}\\ \hline \frac{\partial\hat{G}(z,\rho)}{\partial\rho_{n_a+n_b+1}}\\ \vdots\\ \frac{\partial\hat{G}(z,\rho)}{\partial\rho_{n_a+n_b+n_c}}\end{pmatrix} = \begin{pmatrix}\frac{\partial a(z,\theta_\zeta)^{-1}}{\partial\omega_{n,1}}m(z)B_g(\theta_b)\\ \vdots\\ \frac{\partial a(z,\theta_\zeta)^{-1}}{\partial\omega_{n,n_r}}m(z)B_g(\theta_b)\\ \frac{\partial a(z,\theta_\zeta)^{-1}}{\partial\omega_{n,n_r+1}}m(z)B_g(\theta_b)\\ \frac{\partial a(z,\theta_\zeta)^{-1}}{\partial\zeta_{n_r+1}}m(z)B_g(\theta_b)\\ \vdots\\ \frac{\partial a(z,\theta_\zeta)^{-1}}{\partial\omega_{n,n_r+n_i}}m(z)B_g(\theta_b)\\ \frac{\partial a(z,\theta_\zeta)^{-1}}{\partial\zeta_{n_r+n_i}}m(z)B_g(\theta_b)\\ \hline a(z,\theta_\zeta)^{-1}m(z)\frac{\partial B_g(\theta_b)}{\partial\rho_{n_a+1}}\\ a(z,\theta_\zeta)^{-1}m(z)\frac{\partial B_g(\theta_b)}{\partial\rho_{n_a+2}}\\ \vdots\\ a(z,\theta_\zeta)^{-1}m(z)\frac{\partial B_g(\theta_b)}{\partial\rho_{n_a+n_b}}\\ \hline 0\\ \vdots\\ 0\end{pmatrix}z^{-n_k} = \begin{pmatrix}-a(z,\theta_\zeta)^{-2}\frac{\partial a(z,\theta_\zeta)}{\partial\omega_{n,1}}m(z)B_g(\theta_b)\\ \vdots\\ -a(z,\theta_\zeta)^{-2}\frac{\partial a(z,\theta_\zeta)}{\partial\omega_{n,n_r}}m(z)B_g(\theta_b)\\ -a(z,\theta_\zeta)^{-2}\frac{\partial a(z,\theta_\zeta)}{\partial\omega_{n,n_r+1}}m(z)B_g(\theta_b)\\ -a(z,\theta_\zeta)^{-2}\frac{\partial a(z,\theta_\zeta)}{\partial\zeta_{n_r+1}}m(z)B_g(\theta_b)\\ \vdots\\ -a(z,\theta_\zeta)^{-2}\frac{\partial a(z,\theta_\zeta)}{\partial\omega_{n,n_r+1+n_i}}m(z)B_g(\theta_b)\\ -a(z,\theta_\zeta)^{-2}\frac{\partial a(z,\theta_\zeta)}{\partial\zeta_{n_r+1+n_i}}m(z)B_g(\theta_b)\\ \hline a(z,\theta_\zeta)^{-1}m(z)\frac{\partial B_g(\theta_b)}{\partial\rho_{n_a+1}}\\ a(z,\theta_\zeta)^{-1}m(z)\frac{\partial B_g(\theta_b)}{\partial\rho_{n_a+2}}\\ \vdots\\ a(z,\theta_\zeta)^{-1}m(z)\frac{\partial B_g(\theta_b)}{\partial\rho_{n_a+n_b}}\\ \hline 0\\ \vdots\\ 0\end{pmatrix}z^{-n_k},$$

and

$$\frac{\partial \hat{H}(z,\rho)}{\partial \rho} = \begin{pmatrix} \frac{\partial \hat{H}(z,\rho)}{\partial \omega_{n,1}} \\ \vdots \\ \frac{\partial \hat{H}(z,\rho)}{\partial \omega_{n,n_r}} \\ \frac{\partial \hat{H}(z,\rho)}{\partial \omega_{n,n_r+1}} \\ \frac{\partial \hat{H}(z,\rho)}{\partial \zeta_{n_r+1}} \\ \vdots \\ \frac{\partial \hat{H}(z,\rho)}{\partial \omega_{n,n_r+n_i}} \\ \frac{\partial \hat{H}(z,\rho)}{\partial \zeta_{n_r+n_i}} \\ \hline \frac{\partial \hat{H}(z,\rho)}{\partial \theta_{n_a+1}} \\ \frac{\partial \hat{H}(z,\rho)}{\partial \theta_{n_a+2}} \\ \vdots \\ \frac{\partial \hat{H}(z,\rho)}{\partial \theta_{n_a+n_b}} \\ \hline \frac{\partial \hat{H}(z,\rho)}{\partial \theta_{n_a+n_b+1}} \\ \vdots \\ \frac{\partial \hat{H}(z,\rho)}{\partial \theta_{n_a+n_b+n_c}} \end{pmatrix} = \begin{pmatrix} \frac{\partial a(z,\theta_\zeta)^{-1}}{\partial \omega_{n,1}} m(z) B_h(\theta_c) \\ \vdots \\ \frac{\partial a(z,\theta_\zeta)^{-1}}{\partial \omega_{n,n_r}} m(z) B_h(\theta_c) \\ \frac{\partial a(z,\theta_\zeta)^{-1}}{\partial \omega_{n,n_r+1}} m(z) B_h(\theta_c) \\ \frac{\partial a(z,\theta_\zeta)^{-1}}{\partial \zeta_{n_r+1}} m(z) B_h(\theta_c) \\ \vdots \\ \frac{\partial a(z,\theta_\zeta)^{-1}}{\partial \omega_{n,n_r+n_i}} m(z) B_h(\theta_c) \\ \frac{\partial a(z,\theta_\zeta)^{-1}}{\partial \zeta_{n_r+n_i}} m(z) B_h(\theta_c) \\ \hline 0 \\ \vdots \\ 0 \\ \hline a(z,\theta_\zeta)^{-1} m(z) \frac{\partial B_h(\theta_c)}{\partial \theta_{n_a+n_b+1}} \\ a(z,\theta_\zeta)^{-1} m(z) \frac{\partial B_h(\theta_c)}{\partial \theta_{n_a+n_b+2}} \\ \vdots \\ a(z,\theta_\zeta)^{-1} m(z) \frac{\partial B_h(\theta_c)}{\partial \theta_{n_a+n_b+n_c}} \end{pmatrix} = \begin{pmatrix} -a(z,\theta_\zeta)^{-2} \frac{\partial a(z,\theta_\zeta)}{\partial \omega_{n,1}} m(z) B_h(\theta_c) \\ \vdots \\ -a(z,\theta_\zeta)^{-2} \frac{\partial a(z,\theta_\zeta)}{\partial \omega_{n,n_r}} m(z) B_h(\theta_c) \\ -a(z,\theta_\zeta)^{-2} \frac{\partial a(z,\theta_\zeta)}{\partial \omega_{n,n_r+1}} m(z) B_h(\theta_c) \\ -a(z,\theta_\zeta)^{-2} \frac{\partial a(z,\theta_\zeta)}{\partial \zeta_{n_r+1}} m(z) B_h(\theta_c) \\ \vdots \\ -a(z,\theta_\zeta)^{-2} \frac{\partial a(z,\theta_\zeta)}{\partial \omega_{n,n_r+1+n_i}} m(z) B_h(\theta_c) \\ -a(z,\theta_\zeta)^{-2} \frac{\partial a(z,\theta_\zeta)}{\partial \zeta_{n_r+1+n_i}} m(z) B_h(\theta_c) \\ \hline 0 \\ \vdots \\ 0 \\ \hline a(z,\theta_\zeta)^{-1} m(z) \frac{\partial B_h(\theta_c)}{\partial \theta_{n_a+n_b+1}} \\ a(z,\theta_\zeta)^{-1} m(z) \frac{\partial B_h(\theta_c)}{\partial \theta_{n_a+n_b+2}} \\ \vdots \\ a(z,\theta_\zeta)^{-1} m(z) \frac{\partial B_h(\theta_c)}{\partial \theta_{n_a+n_b+n_c}} \end{pmatrix},$$

with

$$\frac{\partial a(z,\theta_\zeta)}{\partial \omega_{n,i}} = \begin{cases} f_1(\theta_\zeta), & \text{for} \quad i = 1, \ldots, n_r, \\ f_2(\theta_\zeta), & \text{for} \quad i = n_r+1, \ldots, n_r+n_i, \end{cases}$$

and

$$\frac{\partial a(z,\theta_\zeta)}{\partial \zeta_i} = f_3(\theta_\zeta), \quad \text{for} \quad i = n_r+1, \ldots, n_r+n_i.$$

having

$$f_1(\theta_\zeta) = \prod_{i=1}^{n_i}\left(z^2 - 2e^{-\zeta_i\omega_{n,i}h}\cos(\omega_{n,i}\sqrt{1-\zeta_i^2}h)z + e^{-2\zeta_i\omega_{n,i}h}\right)\prod_{\substack{k=1\\k\neq i}}^{n_r}\left(z - \text{sign}(z_k)e^{-\omega_{n,k}^r h}\right)\times$$

$$\ldots \qquad \frac{\partial}{\partial\omega_{n,i}}\left(z - \text{sign}(z_i)e^{-\omega_{n,i}h}\right),$$

$$f_2(\theta_\zeta) = \prod_{\substack{k=1\\k\neq i}}^{n_i}\left(z^2 - 2e^{-\zeta_k\omega_{n,k}h}\cos(\omega_{n,k}\sqrt{1-\zeta_k^2}h)z + e^{-2\zeta_k\omega_{n,k}h}\right)\prod_{j=1}^{n_r}\left(z - \text{sign}(z_j)e^{-\omega_{n,j}^r h}\right)\times$$

$$\ldots \qquad \frac{\partial}{\partial\omega_{n,i}}\left(z^2 - 2e^{-\zeta_i\omega_{n,i}h}\cos(\omega_{n,i}\sqrt{1-\zeta_i^2}h)z + e^{-2\zeta_i\omega_{n,i}h}\right),$$

$$f_3(\theta_\zeta) = \prod_{\substack{k=1\\k\neq i}}^{n_i}\left(z^2 - 2e^{-\zeta_k\omega_{n,k}h}\cos(\omega_{n,k}\sqrt{1-\zeta_k^2}h)z + e^{-2\zeta_k\omega_{n,k}h}\right)\prod_{j=1}^{n_r}\left(z - \text{sign}(z_j)e^{-\omega_{n,j}^r h}\right)\times$$

$$\ldots \qquad \frac{\partial}{\partial\zeta_i}\left(z^2 - 2e^{-\zeta_i\omega_{n,i}h}\cos(\omega_{n,i}\sqrt{1-\zeta_i^2}h)z + e^{-2\zeta_i\omega_{n,i}h}\right).$$

Appendix B.

The optimal procedure consists of two estimations. The final (combined) estimated model is evaluated following the steps:

1. $P_\theta = \left[\sum_{i=1}^{m}\left(P_\theta^{(i)}\right)^{-1}\right]^{-1}$ [17].
2. $\theta_{\text{opt}} = P_\theta\sum_{i=1}^{m}\left(P_\theta^{(i)}\right)^{-1}\theta^{(i)}$ [17].
3. Construct G_{opt} using θ_{opt}.

Here, m is the number of estimations, which in the optimal procedure in two. Furthermore, $P_\theta^{(i)}$ is the covariance matrix of the parameter vector $\theta^{(i)}$ of estimation i. These matrices are given by the Matlab System Identification toolbox. Note that the above steps are also followed to evaluate the estimated damping coefficients from the optimal procedures.

References

[1] F. Galvan and P. Overholt, "The intelligent grid enters a new dimension," *T&D World*, 2014.

[2] D. N. Kosterev, C. W. Taylor, and W. A. Mittelstadt, "Model validation for the August 10, 1996 WSCC system outage," *Trans. Power Syst, vol. 14(3), pp. 967-979*, 1999.

[3] Union for the Coordination of the Transmission of Electricity, "UCTE final report: System disturbance on 4 November 2006," UCTE, Tech. Rep., 2006.

[4] C. Lu, X. Wu, J. Wu, P. Li, Y. Han, and L. Li, "Implementations and experiences of wide-area HVDC damping control in China Southern Power Grid," *Power and Energy Society General Meeting*, 2012.

[5] P. Kundur, M. Klein, G. J. Rogers, and M. S. Zywno, "Application of power system stabilizers for enhancement of overall system stability," *Trans. Power Syst, vol. 4(2), pp. 614-626*, 1989.

[6] J. F. Hauer and J. R. Cresap, "Measurement and modeling of pacific AC intertie response to random load switching," *Transactions on Power Apparatus and Systems, vol. 100(1), pp. 353-359*, 1981.

[7] N. Zhou, J. F. Hauer, and J. W. Pierre, "Initial results in power system identification from injected probing signals using a subspace method," *Trans. Power Syst, vol. 21(3), pp. 1296-1302*, 2006.

[8] B. J. Pierre, F. Wilches-Bernal, D. A. Schoenwald, R. T. Elliott, J. C. Neely, R. H. Byrne, and D. J. Trudnowski, "Open-loop testing results for the pacific DC intertie wide area damping controller," *Manchester PowerTech*, 2017.

[9] S. A. N. Sarmadi and V. Venkatasubramanian, "Inter-area resonance in power systems from forced oscillations," *Trans. Power Syst, vol. 31(1), pp. 378-386*, 2016.

[10] M. Ghorbaniparvar, "Survey on forced oscillations in power systems," *Journal of Modern Power Systems and Clean Energy, vol. 5(5), pp. 671-682*, 2017.

[11] M. Donnelly, D. Trudnowski, J. Colwell, J. Pierre, and L. Dosiek, "RMS-energy filter design for real-time oscillation detection," *Power & Energy Society General Meeting*, 2015.

[12] D. Kosterev, J. Burns, N. Leitschuh, J. Anasis, A. Donahoo, D. Trudnowski, M. Donnelly, and J. Pierre, "Implementation and operation experience with oscillation detection application at Bonneville power administration," *Grid of the Future Symposium*, 2016.

[13] J. F. Hauer and F. Vakili, "An oscillation detector used in the BPA power system disturbance monitor," *Trans. Power Syst, vol. 5(1), pp. 74-79*, 1990.

[14] J. W. Pierre, N. Zhou, F. K. Tuffner, J. F. Hauer, and D. J. Trudnowski, "Probing signal design for power system identification," *Trans. Power Syst, vol. 25(2), pp. 835-843*, 2010.

[15] V. Peric, X. Bombois, and L. Vanfretti, "Optimal multisine probing signal design for power system electromechanical mode estimation," *Hawaii International Conference on System Sciences*, 2017.

[16] T. Söderström and P. Stoica, *System identification.* Prentice Hall, 1989.

[17] L. Ljung, *System identification: theory for the user.* Prentice Hall, 1999.

[18] V. Peric, X. Bombois, and L. Vanfretti, "Optimal signal selection for power system ambient mode estimation using a prediction error criterion," *Trans. Power Syst, vol. 31(4), pp. 2621-2633*, 2016.

[19] M. Baudette, M. Castro, T. Rabuzin, J. Lavenius, T. Bogodorova, and L. Vanfretti, "OpenIPSL: Open-Instance Power System Library - Update 1.5 to "iTesla Power Systems Library (iPSL): A Modelica library for phasor time-domain simulations"," *SoftwareX, vol. 7, pp. 2352-7110*, 2018.

[20] S. Boersma, "https://github.com/sboersma3/SysIdInDymola," 2019.

[21] M. Baur, M. Otter, and B. Thiele, "Modelica Libraries for Linear Control Systems," *Proceedings of the 7th International Modelica Conference*, 2009.

[22] L. Dosiek, "On the Cramér–Rao bound of power system electromechanical mode meters," *Trans. Power Syst, vol. 34(6), pp. 4674-4683*, 2019.

[23] L. Vanfretti, S. H. Olsen, V. S. N. Arava, G. Laera, A. Bidadfar, T. Rabuzin, S. H. Jakobsen, J. Lavenius, M. Baudette, and F. J. Gòmez-Lòpez, "An open data repository and a data processing software toolset of an equivalent Nordic gridmodel matched to historical electricitymarket data," *Data in Brief, vol. 11, pp. 349-357*, 2017.

[24] J. C. Gonzalez-Torres, J. Mermet-Guyennet, S. Silvant, and A. Benchaib, "Power system stability enhancement via VSC-HVDC control using remote signals: application on the Nordic 44-bus test system," *International Conference on AC and DC Power Transmission*, 2019.